Published in final edited form as:
J Phys Chem A. 2011 April 28; 115(16): 4031–4041. doi:10.1021/jp109786w.

Lanthanide Sensitization in II–VI Semiconductor Materials: A Case Study with Terbium (III) and Europium (III) in Zinc Sulfide Nanoparticles

Prasun Mukherjee[1], **Chad M. Shade**[1], **Adrienne M. Yingling**[1], **Daniel N. Lamont**[1], **David H. Waldeck**[1,*], and **Stéphane Petoud**[1,2,*]

[1]Department of Chemistry, University of Pittsburgh, Pittsburgh, PA 15260

[2]Centre de Biophysique Moléculaire, CNRS UPR 4301, rue Charles Sadron, 45071 Orléans, France

Abstract

This work explores the sensitization of luminescent lanthanide Tb^{3+} and Eu^{3+} cations by the electronic structure of zinc sulfide (ZnS) semiconductor nanoparticles. Excitation spectra collected, while monitoring the lanthanide emission bands, reveals that the ZnS nanoparticles act as an antenna for the sensitization of Tb^{3+} and Eu^{3+}. The mechanism of lanthanide ion luminescence sensitization is rationalized in terms of an energy and charge transfer between trap sites and is based on a semi-empirical model, proposed by Dorenbos and coworkers, 1⁻6 to describe the energy level scheme. This model implies that the mechanisms of luminescence sensitization of Tb^{3+} and Eu^{3+} in ZnS nanoparticles are different; namely Tb^{3+} acts as a hole trap, while Eu^{3+} acts as an electron trap. Further testing of this model is made by extending the studies from ZnS nanoparticles to other II–VI semiconductor materials; namely, CdSe, CdS, and ZnSe.

Introduction

Historically, luminescent lanthanides have been extensively used as phosphors, and more recently they have attracted interest as a new class of luminescent probes and sensors for biological applications. 7⁻13 Lanthanides have a number of luminescence properties that make them an attractive alternative to organic fluorophores in bioanalytical applications and biological imaging. Whereas typical organic fluorophores are prone to photobleaching mechanisms, lanthanide luminescence is highly resistant to photobleaching and hence allows longer experiment times or their repetition. The sharp atom-like lanthanide emission bands and the negligible overlap between the bands of different lanthanide ions makes them promising candidates for multiplex biological assays through spectral discrimination or for barcode types of applications. 14 Moreover, the long lanthanide luminescence lifetimes (~ ms time domain for lanthanide emitting in the visible) allows their signal to be distinguished from the background autofluorescence of biological media (~ ns time domain) through temporal discrimination for improved detection sensitivity.

A major requirement for the use of lanthanides as biological imaging agents is the detection sensitivity they can provide which includes the emission of a sufficient number of photons in order to obtain good detection sensitivity. The direct excitation of lanthanides is inefficient because most of the interesting f–f transitions are Laporte forbidden. 15,16 As a

*To whom correspondence should be addressed..

consequence, the molar extinction coefficients of lanthanide ions are very low 17 (≤ 10 $M^{-1}cm^{-1}$ as opposed to 10^4–10^5 $M^{-1}cm^{-1}$ for typical organic fluorophores). The low number of absorbed photons will result in the low number of emitted photons. To overcome this limitation, the concept of sensitization through an antenna effect has been established. 8·18−28 In this process, photons from the excitation light are absorbed by a chromophore with high extinction coefficient that transfers the energy to the accepting levels of the lanthanide ions, thus creating a high population of electronically excited lanthanide ions and enhancing the amount of luminescent photons. In addition to efficient energy pumping by this antenna effect, it is also important to prevent the quenching of lanthanide ion excited states by nonradiative energy transfer to the overtones of high frequency vibrational modes such as −OH, −NH and −CH. 29 For applications under biological conditions, it is especially important to protect the lanthanide ions from the water molecules.

Semiconductor nanoparticles that contain lanthanide ions are advantageous for biological applications over the undoped nanoparticles because the sharp emission signal corresponding to each lanthanide ion has a unique spectroscopic signature for spectral identification and unambiguous identification. Depending on the lanthanide cations, there is a broad choice of emission wavelength throughout the entire visible and near IR spectral regions. The near IR luminescence of lanthanide cations is of special benefit for biological applications because i) the absence of native autofluorescence of tissues in the near IR region, a good signal to noise ratio is obtained for more sensitive detection and ii) near IR photons can cross significant depths of tissues for potential non-invasive investigation. Recently Chengelis et. al. reported on the incorporation of terbium ions (Tb^{3+}) in CdSe nanoparticles. 30 Although Tb^{3+} luminescence sensitization was observed for the CdSe/Tb^{3+} system, its emission was obscured by the more intense CdSe bandgap emission in steady-state mode and a time-gated method was required to specifically identify the Tb^{3+} luminescence. From the excitation spectrum, collected upon monitoring the 545 nm centered Tb^{3+} emission signal, it is evident that part of the excitation energy is transferred from the CdSe nanoparticle states to the accepting energy levels of Tb^{3+} ions demonstrating that the electronic structure of the nanoparticle can act as an antenna. While the CdSe/Tb^{3+} system demonstrates the use of the nanoparticles as an antenna, it has intrinsic limitations, namely, the efficiency of CdSe in sensitizing Tb^{3+} luminescence was low, and the Cd and Se components of the nanoparticles are toxic, thus limiting their applicability for studying biological systems and for diagnostic purposes. To overcome these two drawbacks, we have created a ZnS/Tb^{3+} nanoparticle system, in which the individual constituents are non-toxic or less toxic and more environmentally friendly. Moreover, as the bulk band gap of ZnS is larger than that of CdSe (3.6 eV as opposed to 1.7 eV), 31 the electronic structure of ZnS is expected to sensitize lanthanides more efficiently than CdSe because it ensures a more favorable match of lanthanide acceptor energy levels with respect to the nanoparticle donating energy levels. 5 This work reports results on ZnS nanoparticles containing three different lanthanides: two visible-emitting lanthanides, Tb^{3+} and Eu^{3+} in ZnS nanoparticles, and corresponding control experiments with Gd^{3+} (which does not have accepting electronic levels in the relevant energy range) incorporated. ZnS nanoparticle systems without lanthanides were also studied for comparison. Both steady-state and time-resolved luminescence measurements demonstrate that ZnS acts as an efficient antenna to sensitize Tb^{3+} and Eu^{3+} luminescence. A comparison with other II–VI materials; (namely, Tb^{3+} incorporated in CdSe, CdS and ZnSe), is made in order to elucidate the energy transfer mechanism between the lanthanide and the nanoparticle host.

Understanding the mechanism of lanthanide luminescence sensitization is of main importance for controlling the performance and properties of novel optical materials. Because lanthanide ions behave as hard acids, they bind strongly to hard bases, following the preference order O>N>S. Various researchers have devoted considerable effort to

understanding and exploiting the mechanisms for the luminescence sensitization of lanthanide in semiconductor materials. Some of the discussed mechanisms are based on a defect related Auger transition model, 32–34 a resonant energy transfer model, 35 bound exciton models 27,36 and shallow donor (or acceptor) models. 37 It is generally believed that exciton recombination plays a key role in the luminescence sensitization of rare earth ions. Although a number of researchers have discussed lanthanide luminescence in bulk semiconductors 38–48 and semiconductor nanoparticles, 49–61 the mechanism of lanthanide luminescence sensitization is still not fully elucidated and does not allow the synthesis of lanthanide-based nanomaterials with predictable properties. The mechanism of Tb^{3+} luminescence sensitization in bulk ZnS has attracted considerable attention. For example, Anderson 26 finds that the process includes (a) a donor level related to Tb^{3+} [$6s^2 5d^1$] that lies 0.4 eV below the conduction band; the $4f^8$ levels were assumed to be located somewhere below the valence band, (b) a hole trap that lies 1.02 eV above the valence band (assumed to be a copper-related site), 62,63 and (c) that the excitation of the $4f^8$ electronic system occurs during recombination of the electron-hole pair in these traps. While these efforts provide a useful framework for the current studies, the luminescence sensitization of Tb^{3+} and Eu^{3+} in ZnS nanoparticles is not well understood. Previous studies have been limited by an inability to identify the location of lanthanide ground and excited states with respect to the valence and conduction bands of the semiconductor materials. In this work, the nature of sensitization in the ZnS nanoparticles is discussed in light of the model proposed by Dorenbos, 1–6 for the relative energetics of the lanthanide ions in the host semiconductor.

Materials and Methods

Chemicals

Trioctylphosphine [TOP] (90%), zinc stearate (tech.), octadecene (90% tech.), and tetracosane (99%) were purchased from Sigma-Aldrich-Fluka. Chloroform was purchased from J. T. Baker. Sulfur, toluene, and methanol were purchased from Fisher Scientific. Terbium (III) nitrate (99.9%) was purchased from Strem, europium (III) nitrate (99.99%) was purchased from Aldrich, and gadolinium (III) nitrate (99.99%) was purchased from Alfa Aesar. In all cases, hydrated lanthanide salts were used. n-Hexane and 1-octanol were purchased from Acros, and ethyl acetate was purchased from EMD. Argon gas was purchased from Valley National. All chemicals were used as purchased without purification, except toluene, which was distilled over sodium under nitrogen.

Nanoparticle Synthesis

All ZnS nanoparticle systems were synthesized using a non-coordinating solvent system consisting of octadecene and tetracosane. Zinc stearate and lanthanide nitrate salts were used as cation precursors and elemental sulfur served as the anion precursor. Tetracosane (4.0 g), octadecene (3.0 mL), and 0.68 mmol of zinc stearate were loaded into a three neck round bottom flask and heated to 350 °C while stirring under nitrogen. The lanthanide stock solution (0.12 mmol lanthanide nitrate dissolved in a combination of octadecene and trioctylphosphine oxide) was injected after approximately two hours of heating and allowed to stir within the reaction mixture for at least 30 minutes. The sulfur stock solution (sulfur powder dissolved in octadecene) was injected approximately 1 hour after the lanthanide stock solution. The reaction temperature was then decreased to a value between 270 °C and 300 °C for the duration of nanocrystal growth. Aliquots of sample were removed at varying growth times. The resulting nanoparticles were then redispersed in an appropriate solvent for spectroscopic analysis.

ZnS nanoparticles without lanthanides incorporated were prepared using the methods described above, however the zinc stearate precursor was increased to 0.80 mmol and the lanthanide stock solution preparation was omitted.

Steady-state Optical Measurements

Steady-state absorption spectra were obtained on an Agilent 8453 UV-visible spectrophotometer with 1-nm resolution. Steady-state excitation and emission spectra were recorded using a Jobin Yvon Horiba Fluorolog-322 with a 5-nm bandpass; spectra were corrected for excitation and emission (lamp, detector and monochromator). A 1-cm pathlength quartz cuvette was used for the measurements. All measurements were performed at room temperature.

Quantum Yields

Absorption spectra were recorded on either a Perkin-Elmer Lambda 9 Spectrometer coupled to a personal computer using software supplied by Perkin-Elmer or on an Agilent 8453 UV-visible spectrophotometer. Quantum yields were recorded by the relative method using references. Steady-state luminescence quantum yields were measured using quinine sulfate reference solution (solvent H_2SO_4 1N, Φ=0.546). 64 Time-gated luminescence quantum yields were measured using [Tb(H_{22}IAM)] reference solution (solvent water, Φ=0.59). 65 Spectra were corrected for the instrumental response.

The quantum yields were calculated using the following (equation 1):

$$\frac{\Phi_x}{\Phi_r}=\frac{A_r(\lambda_r)\cdot I(\lambda_r)\cdot \eta_x^2\cdot D_x}{A_x(\lambda_x)\cdot I(\lambda_x)\cdot \eta_r^2\cdot D_r} \quad (1)$$

where subscript r stands for the reference and×for the sample; A is the absorbance at the excitation wavelength, I is the intensity of the excitation light at the same wavelength, η is the refractive index (η = 1.333 in water, η = 1.496 in toluene, η = 1.446 in chloroform) and D is the measured integrated luminescence intensity. ZnS systems (λ_{ex} = 315, 320 and 325 nm) were measured in chloroform whereas ZnSe (λ_{ex} = 315, 320 and 325 nm) and CdSe (λ_{ex} = 300, 305 and 310 nm) systems were measured in toluene.

Lanthanide-centered quantum yields for ZnSe/Ln^{3+} and CdSe/Ln^{3+} were collected with the fluorimeter in time-gated mode whereas the contribution from lanthanide-centered emission was discriminated spectrally from the overall quantum yield. For the ZnS/Ln^{3+} systems calculations were performed by integrating the narrow emission bands arising from the lanthanide cations in steady-state mode.

Time-gated Measurements

Time-gated excitation and emission spectra were collected with a Varian Cary Eclipse fluorescence spectrophotometer with 10 nm and 20 nm bandpass for Tb and Eu samples respectively. The spectra were acquired with a delay time and a gate time of 0.2 ms and 5 ms, respectively. Using such a delay time, only lanthanide sharp bands are expected to appear in the spectra without any contribution from shorter lived nanoparticle bandgap emission. Both excitation and emission filters were set in auto mode in the software. All measurements were performed at room temperature.

Time-resolved Measurements

The time-resolved luminescence decay kinetics was measured using the time-correlated single-photon counting (TCSPC) technique. Samples were excited with the frequency doubled output (centered at ~300 nm) of a synchronously pumped cavity dumped dye laser (Coherent Model 599) using rhodamine 6G as the gain medium; emission from the sample was collected at different wavelengths using a monochromator. The instrument response function had a full-width–at-half-maximum (FWHM) of ~40 ps. A 1-cm pathlength quartz cuvette was used for all the time-resolved measurements. All measurements were performed at room temperature. Experiments were done with a 1 MHz laser repetition rate. Lifetime values were found to be similar with 125 kHz (for ZnS/Tb) and 300 kHz (for ZnS/Gd and ZnS) repetition rate; these measurements were done at selected wavelengths. Lifetime decay traces were fitted by iterative reconvolution method with IBH DAS 6 decay analysis software.

The Tb^{3+} and Eu^{3+} luminescence lifetime measurements were performed by excitation of solutions in 1 mm quartz cells (NSG Precision Cells, Inc.) using either a xenon flash lamp or a Nd-YAG Continuum Powerlite 8100 laser (354 nm, third harmonic) as the excitation source. Emission was collected at a right angle to the excitation beam, and wavelengths were selected by means of the Spex FL1005 double monochromator or a Spectral Products CM 110 1/8 meter monochromator. The signal was monitored by a Hamamatsu R928 photomultiplier tube coupled to a 500 MHz bandpass digital oscilloscope (Tektronix TDS 620B). Signals from > 500 flashes were collected and averaged. Luminescence lifetimes were averaged using samples from several different batches. Luminescence decay curves were imported into Origin 7.0, and analyzed using the Advanced Fitting Tool.

Results and Discussion

HRTEM Imaging

High resolution Transmission Electron Microscopy (HRTEM) images were obtained using a JEOL-2100 CF instrument operating between 120 kV and 200 kV. A representative TEM image is shown in figure 1. The size distribution of ZnS:Tb nanoparticles was calculated using Image J software and found to be 3.3 ± 0.4 nm in average diameter. Both the stoichiometry (lanthanide to zinc ratio) and the location of the lanthanides in the nanoparticles are not yet fully quantified. These data will be reported in a more comprehensive future study that will address the stoichiometry and the relative importance of the lanthanide locations – on the surface or in the bulk of the nanoparticles.

Absorption Spectra

Representative absorption spectra of ZnS nanoparticles dissolved in chloroform are shown in figure 2 for two different growth times. The absorption spectra reveal characteristic bands centered at ~290 nm and ~360 nm. The band with an apparent maximum at ~290 nm shows a small dependence on growth time and is attributed to the lowest energy exciton band of the nanoparticle. The ~360 nm band is probably associated with a transition involving a trap state. The assignment of the ~290 nm band is corroborated by a simple estimation of the nanoparticle band gap, using a method proposed by Brus 66 (equation 2), and found to be ~4.2 eV, corresponding to a ~290 nm band gap transition. In this model the change in bandgap with nanoparticle size is given by

$$E_g(\text{nano}) \approx E_g(\text{bulk}) + \frac{\hbar^2\pi^2}{2R^2}\left[\frac{1}{m_e} + \frac{1}{m_h}\right] - \frac{1.8e^2}{\varepsilon R} \quad (2)$$

Assuming E_g(bulk) = 3.6 eV, R = 1.65 nm (see above), $m_e = 0.25m_0$, $m_h = 0.59m_0$, ε = 8.3, E_g(nano) = 4.2 eV. The effective mass and dielectric constant values were adopted from the work by Murphy and coworkers. 67 We assign the long wavelength tail to the contribution from various surface states of the nanoparticles *(vide infra)*.

Luminescence Spectra

Figure 3 shows steady-state luminescence excitation and emission spectra for the lanthanide incorporated ZnS nanoparticles and for undoped ZnS nanoparticles (NP) without lanthanide ions, in $CHCl_3$. The spectra correspond to ~20 minutes NP growth time; the spectra corresponding to the analysis of the samples obtained after 1 minute growth times are similar.

ZnS/Tb Spectra—Figure 3B shows emission spectra for ZnS/Tb. For λ_{ex} = 300 nm, λ_{em} bands were identified at ~ 410 nm (ZnS band), 490 nm, 545 nm, 585 nm, and 620 nm (Tb^{3+} sharp bands); for λ_{ex} = 375 nm, λ_{em} bands were assigned at ~ 455 nm (ZnS band), 490 nm (weak Tb^{3+} band), and 545 nm (Tb^{3+} band); and for λ_{ex} = 440 nm, a λ_{em} band was assigned at ~ 510 nm (ZnS band). An excitation wavelength dependence (red edge effect) is observed, i.e., with increase in λ_{ex} the emission band position shifts towards the red.

The excitation spectra (Figure 3A) also depend on λ_{em}. For λ_{em} = 410 nm (ZnS emission), the λ_{ex} bands were identified at ~ 260 nm and 350 nm; for λ_{em} = 450 nm (ZnS emission), the λ_{ex} bands were assigned at ~ 270 nm and 375 nm; and for λ_{em} = 545 nm (Tb^{3+} emission), a broad λ_{ex} feature appeared. To examine whether this wavelength dependence reflects size heterogeneity of the sample, efforts were made to improve the sample's size distribution. Thus centrifugation was performed at 20,000 rpm for 2 hours, a chemical purification by solvent precipitation method (see supporting information) was used, and the nanoparticle samples were dialyzed. None of these three methods yielded any noticeable change in the excitation wavelength dependent behavior. Based on these studies, the excitation wavelength dependent emission spectra are taken to reflect the energy distribution of surface states on the nanoparticles.

Sensitization of the lanthanide emission is evident in the steady-state emission spectra. Interestingly, the lanthanide emission intensity displays a wavelength dependence; when exciting the sample at 300 nm, terbium (Tb^{3+}) bands at ~490 nm and ~545 nm are clearly identifiable; whereas a 375 nm excitation results only in a weak Tb^{3+} emission. Excitation with 440 nm light results in no observable Tb^{3+} sensitization in the steady-state mode, however a weak Tb^{3+} sensitization can be observed in time-gated mode. This dependence on excitation energy correlates with the energy level mismatch between the donating excited states of ZnS nanoparticles and the accepting levels of Tb^{3+} ions (*vide infra*).

The broad excitation spectrum, with an absence of any atom-like band upon monitoring the Tb^{3+} emission, clearly indicates that the electronic structure of ZnS nanoparticles act as an antenna for the Tb^{3+} sensitization (and not from direct excitation of the lanthanide cations). Additional evidence for this interpretation has been obtained from the time-gated spectrum (*vide infra*).

The broad nature of the nanoparticle emission band indicates that the spectrum consists primarily of surface states or results from the combined emission of core states of variously sized nanoparticles. Peng and coworkers 68 have reported that the bandgap photoluminescence of ZnS nanoparticles is often mixed with a deep trap tail; namely a bandgap photoluminescence at ~310 nm (FWHM of 10–12 nm) and a broad band ~380 nm deep trap emission. A similar broad emission from ZnS nanoparticle surface states was also reported by Chen and coworkers. 69 Also Murphy and coworkers 67 reported a broad

emission band centered at ~435 nm upon excitation of 5 nm ZnS nanoparticles at 270 nm, and have attributed that emission to sulfur vacancies, more generally to shallow electron traps. Although the band maximum is somewhat shifted, this reported blue emission is qualitatively similar to that observed in this study while exciting the sample at ~300 nm. While the chemical nature of the surface states remains unclear, it seems evident that they play a significant role in broadening the emission spectrum. The observation that 1 minute and 20 minutes growth time samples have identical emission spectra indicates that the surface state distribution does not change with growth time for the synthetic parameters that were utilized here.

ZnS/Eu Spectra—Figure 3D shows the steady-state emission spectra for ZnS/Eu^{3+}. For λ_{ex} = 300 nm, a λ_{em} band was assigned at ~ 460 nm (ZnS band); for λ_{ex} = 375 nm, a λ_{em} band was found at ~ 455 nm (ZnS band); and for λ_{ex} = 440 nm, a λ_{em} band was found at ~ 510 nm (ZnS band). These materials also display a red edge effect. Although this observation is qualitatively similar to the spectral change observed for the ZnS/Tb samples, some differences are evident; in particular, the emission spectrum for λ_{ex} = 300 nm has a similar emission band maximum as that for the spectrum with λ_{ex} = 375 nm. The absence of broad emission with band maximum centered at ~520 nm upon exciting the sample at ~300 nm indicates that the samples under investigation in the present work do not have significant emission from Eu^{2+} (See reference 70 for more detail).

Figure 3C shows the excitation spectra for ZnS/Eu^{3+}. For λ_{em} = 410 nm (ZnS emission), λ_{ex} bands were identified at approximately 255 nm, 270 nm, and 350 nm; for λ_{em} = 450 nm (ZnS emission), λ_{ex} bands were assigned at approximately 260 nm, and 370 nm; and for λ_{em} = 620 nm (attributed to Eu^{3+} emission), a λ_{ex} band appeared at approximately 360 nm, with a broad excitation band centered at approximately 510 nm (assigned to a charge transfer transition from anion valence band to Eu^{3+} ions, *vide infra*).

The luminescence signal from the Eu^{3+} is not clearly evident in the steady-state spectra; however, it becomes prominent in time-gated mode (*vide infra*). Qualitatively, the less intense Eu^{3+} emission indicates that the ZnS nanoparticles are less efficient in sensitizing Eu^{3+}, as compared to the corresponding Tb^{3+} system. The broad band located on the emission spectrum probably reflects the contribution from surface states, as was discussed previously for ZnS/Tb samples. Similar to the observation found in ZnS/Tb system, no shift in band positions was observed in the emission spectra for 1 minute and 24 minutes growth time samples, suggesting that the surface states play an important role.

ZnS/Gd Spectra—Figures 3E and 3F show the excitation and emission spectra of ZnS/Gd. Other than the lack of Tb^{3+} emission bands, the nanoparticle spectra recorded on ZnS/Gd samples (exclusive of the ions 4f emission bands) were found to be very similar to those recorded for the ZnS/Tb samples in terms of band positions, excitation wavelength dependence and broadness of the spectra, indicating that luminescence sensitization of Tb^{3+} has a negligible impact on the nanoparticle emission in ZnS/Tb samples.

ZnS Spectra—Figures 3G and 3H show the excitation and emission spectra if ZnS. These spectra show an excitation wavelength dependence (red edge effect) that is similar to that observed for the ZnS/Tb and ZnS/Gd samples, indicating that the red edge effect arises from an intrinsic property of the ZnS nanoparticles and is not caused by the lanthanide ion. The broad nature of nanoparticle emission indicates that the spectrum is strongly influenced by the surface states, as are the samples where lanthanide ions are incorporated in the nanoparticle.

Time-gated Excitation and Emission Spectra

Representative time-gated excitation and emission spectra of ZnS/Tb (1 minute growth time) and ZnS/Eu (24 minutes growth time) nanoparticle samples in $CHCl_3$ are shown in figure 4. The attempt to collect spectra for the ZnS/Gd and the ZnS nanoparticles under the same conditions only showed the background signal.

These spectra reveal that the electronic levels of ZnS nanoparticles can be used to sensitize the Tb^{3+} and Eu^{3+} emission. Sharp lanthanide emission bands were clearly visible for both the ZnS/Tb and the ZnS/Eu samples. For the ZnS/Tb sample, the bands with apparent maxima at 490 nm, 545 nm, 585 nm, and 620 nm were assigned to transitions from $^5D_4$ to $^7F_6$, $^7F_5$, $^7F_4$, $^7F_3$ respectively. For the ZnS/Eu sample, the bands at 590 nm, 616 nm, and 696 nm were assigned to transitions from $^5D_0$ to $^7F_1$, $^7F_2$, $^7F_4$ respectively.

The excitation spectra, recorded upon monitoring the lanthanide emission, reveal a broad excitation spectrum that is similar to the one recorded for the ZnS nanoparticles, upon monitoring their emission at either 410 nm or 450 nm. These results imply that the same energy route is used to sensitize emission of the ZnS and lanthanide emission, proceeding by energy transfer from the electronic states of the ZnS to the accepting levels of Tb^{3+} or Eu^{3+}. This conclusion is confirmed by the absence of sharp intra-configurational f–f bands in the excitation spectra, which would indicate direct excitation of lanthanide ions. It is important to note that the energy transfer from the 4f-5d excitation band of Tb^{3+}, and the charge transfer band of Eu^{3+}, are broad excitation bands and may contribute to the excitation spectrum. The 4f-5d excitation band in Tb^{3+} arises at ~4.8 eV, 2 and for Eu^{3+} (in sulfide compounds) the charge transfer band from the anion valence band to Eu^{3+} occurs at ~2.2 eV. 4 Although excitation at higher energies cannot rule out the possibility of some partial energy transfer from Tb^{3+} 4f-5d excitation band, the strongest Tb^{3+} and Eu^{3+} luminescence arises from exciting the sample in the 280 nm to 350 nm window and argues in favor of the ZnS bandgap excitation being the dominant excitation pathway. However, the luminescence of Tb^{3+} decreases more sharply with increasing wavelength than does that of Eu^{3+} (*vide infra*, see figure 7 and table 4S), suggesting that the charge transfer excitation from the anion valence band to Eu^{3+} can also play a role in the Eu^{3+} sensitization. It is important to appreciate that the charge transfer band in Eu^{3+} is weak and its contribution alone cannot account for the sensitization; in particular, that arising from exciting the sample at higher energies.

ZnS Luminescence Lifetime Measurements

Luminescence lifetime parameters for the different systems studied are summarized in table 1S (see supporting information). Table 1S shows values for all parameters in a sum of three exponentials varied in the fitting procedure. To see any obvious trend in the individual lifetime components, the decay data were also fit to a sum of exponentials with lifetime components fixed and varying only the amplitudes (table 2S, see supporting information). This procedure gives rise to somewhat lesser quality fits, as judged by the relative χ^2 value being higher; however they are adequate and reveal a clear relationship between lifetime components in the different systems. Note that the average lifetime remains relatively unchanged while varying all parameters versus fixing the lifetime components in the fitting procedure. Some representative luminescence decays for 1 minute growth time samples are shown in figure 5.

ZnS/Tb Samples—The samples obtained with 1 minute and 20 minutes growth time behave similarly in terms of the decay kinetics. The experimental lifetime decays were typically fitted with the sum of three decaying exponentials, with a subnanosecond component which comprises ~60% of the emission, a 2–3 ns component with ~30%

contribution, and the longest time component (~10 ns) with an amplitude of ≤~10%. The average lifetime increases continuously with increasing λ_{em}, which indicates that the emission band shifts with time. Attempts were made to monitor the Tb^{3+} emission by lowering the repetition rate to ~100 kHz and increasing the full time window to 5 microseconds; in all cases only the ZnS emission was significant and no longer time component, which might be related to the Tb^{3+} emission, was observed. At all wavelengths, only the ZnS emission is important. Long lived Tb^{3+} emission appears as a baseline as shown in upper left panel in figure 5 at 545 nm.

ZnS/Eu Samples—ZnS/Eu behaves differently compared to all other systems. Namely, the longer lifetimes are more dominant in this sample and the amplitude of the subnanosecond component is much lower. This result suggests that a different energy transfer mechanism may take place. Balandin and coworkers 71 used a theoretical investigation of ZnO quantum dots to predict an increase in radiative lifetime for surface bound ionized acceptor-exciton complex, as compared to the lifetimes of confined excitons and surface bound ionized donor-exciton complexes. Such a type of complex would give rise to an increase in quantum yield. A comparison of the overall quantum yield of ZnS/Eu^{3+} (0.27 ± 0.02) to that of ZnS/Tb^{3+} (0.12 ± 0.03) corroborate this conclusion. The lack of a long-lived baseline in the ZnS/Eu sample, as compared to the ZnS/Tb sample, reflects the decreased luminescence of the Eu bands in the steady-state spectra (Figure 3D).

ZnS/Gd Samples—Because of an energy level mismatch between the donating energy levels of the nanoparticles and the Gd^{3+} accepting levels no Gd^{3+} luminescence is observed. The fact that the ZnS/Gd^{3+} sample's nanoparticle emission is very similar to the ZnS emission of the ZnS/Tb^{3+} shows that the ZnS properties are not sensitive to the presence and nature of the lanthanide cations.

ZnS Samples—The average lifetime of the ZnS sample is comparable to that of the corresponding value in the presence of Tb^{3+} and Gd^{3+}. The ZnS sample's emission lifetime depends on λ_{em} in a fashion which is similar to that found for the lanthanide containing nanoparticles. Thus the emission wavelength dependence appears to be an intrinsic property of the nanoparticles and is not associated with the presence of lanthanide ions (Tb^{3+}, Eu^{3+} and Gd^{3+}) in the system. The origin of the shift might be caused by decays from different donor-acceptor pairs that vary in distance, that is, close pairs emit with faster lifetime at higher energy and the distant pairs emit at lower energy. 72

Lanthanide Ion Luminescence Lifetime Measurements

The luminescence lifetimes of the lanthanide cations were recorded using a low repetition rate Nd-YAG laser based setup. Experimental luminescence signals were fitted best by a biexponential decay for Tb^{3+} and Eu^{3+}. For ZnS/Tb^{3+}, the luminescence lifetime values were found to be 0.92 ± 0.01 ms and 2.50 ± 0.06 ms, whereas, for ZnS/Eu^{3+}, the corresponding values were 2.0 ± 0.01 ms and 3.6 ± 0.2 ms. The lifetimes for the Tb^{3+} emission band are similar to those observed for $CdSe/Tb^{3+}$ in a previous study. 30 Two components could arise from different locations of the lanthanide ions in the nanoparticles; e.g. Tb^{3+} in the core of the ZnS nanoparticles may be better protected and have a longer luminescence lifetime, whereas the shorter lifetime component may originate from the surface located Tb^{3+} which experiences more solvent quenching. Examples of lifetime values for molecular complexes with well protected Tb^{3+} and Eu^{3+} cation coordination sites are 1.3 ms and 0.78 ms respectively. 73 The longer lifetime values recorded in the nanoparticle samples suggest that the lanthanide ions are better protected from quenching through vibrations located in solvent (and in the organic sensitizer for molecular complexes) when in the nanoparticles, as was reported previously by Chengelis et. al. for $CdSe/Tb^{3+}$. 30

A Mechanism for Sensitization of Lanthanide Luminescence

This section considers the possibility of Förster (dipole-dipole interaction) and Dexter (exchange interaction) electronic energy transfer mechanisms in the studied systems, but argues that a different mechanism operates.

The rate of energy transfer under the Förster formulation depends on (a) the spectral overlap of donor and acceptor (J_F), (b) the donor luminescence quantum yield, (c) the donor luminescence lifetime, (d) the relative orientation of donor and acceptor transition dipoles, and (e) the distance between donor and acceptor. Most of the lanthanide transitions (dipolar electric) are formally forbidden and thus have a low oscillator strength and a low energy transfer rate by the Förster mechanism. The Förster overlap integral is $J_F \sim 10^{-19}$–10^{-20} $M^{-1}cm^3$ for the systems studied here, whereas the typical value of J_F for organic fluorophores is on the order of 10^{-13}–10^{-15} $M^{-1}cm^3$. 74 Assuming a $\Phi_D = 0.2$, one calculates an R_0 of ~ 2.5 Å for a lanthanide, which should be compared to a value of $R_0 = 25$ Å for a typical organic fluorophore. The ratio of the rate of energy transfer for organic fluoropohores in comparison to the ZnS/Tb^{3+} nanoparticle samples is ~ 10^6. Based on this estimate, we conclude that the Förster mechanism is less likely to play a significant role in the energy transfer process for the systems investigated in the present study. More straightforward evidence against the operation of the Förster energy transfer mechanism can be established from a comparison of J_F and R_0 values in the different systems studied (see Table 3S in supporting information). The Förster model predicts that the Eu^{3+} sensitization should be larger than Tb^{3+} in ZnS nanoparticles for a given distance, by ~ 3 times; in contrast, the experiments show that Tb^{3+} is at least two-fold more luminescent than Eu^{3+} (*vide infra*). In addition, a comparison of the host nanoparticles (ZnS, ZnSe, CdS, CdSe) indicates that the rate of energy transfer to Tb^{3+} should be very similar in ZnS and CdS; however, experiments demonstrate that ZnS is more efficient than CdS in sensitizing Tb^{3+} luminescence (figure 6). 75

The rate of energy transfer for the Dexter formulation depends on (a) the spectral overlap of donor emission and acceptor absorption (J_D) and (b) the electronic coupling factor. The Dexter mechanism can account for energy transfer involving forbidden transitions. The fact that the calculated J_D values are very similar in the different systems indicates that the experimental trend in energy transfer rates among the different nanoparticles can only be explained by a concomitant change in the electronic coupling parameter. While this possibility cannot be excluded, it seems unlikely. Thus, it seems that both the Förster and Dexter energy transfer mechanisms play a negligible role in the energy transfer mechanism of the studied systems.

A number of other plausible mechanisms for luminescence sensitization in rare earth ions in semiconductors have been proposed. For example, Klik et al., in the context of InP/Yb^{3+}, 28 rationalized Yb^{3+} sensitization in InP by the mechanism: (a) excitation of the semiconductor from the valence band to conduction band, (b) capturing of a free electron at a Yb^{3+} related trap located at 0.03 eV below the conduction band, (c) generation of an electron-hole pair on the trap, and (d) non-radiative recombination of electron-hole pair being the excitation source of the Yb^{3+}, thus generating the Yb^{3+} emission. This model was based on earlier studies by Palm et al., 27 Takahei and coworkers, 76·77 Thonke et. al. 78 and Needels et. al. 79 In molecular systems, Lazarides has discussed a redox-based energy transfer mechanism in the context of molecular d–f complexes. 80 Mechanisms of this type require a detailed knowledge of the dopant energy levels in the host semiconductor.

Although much has been discussed about the lanthanide sensitization in semiconductor materials, considerably less is known about the energy level positions of lanthanide ions in the host material. 81⁻85 The location of dopant ion energy levels with respect to the valence

and conduction bands of the host lattice is of extreme importance, because it is useful for predicting the luminescence properties, and the charge trapping and de-trapping kinetics. Recently, Dorenbos 1⁻6 has addressed the problem of locating lanthanide impurity levels in a host crystal semi-empirically and developed a model that relies on three host dependent parameters: (a) the charge transfer energy from the anion valence band to Eu^{3+}, (b) the redshift of the first 4f to 5d transition in appropriate lanthanide ions, and (c) the band gap of the semiconductor material. The fundamental assumptions in this method are that the binding energies of the 4f electrons follow a universal trend and that the charge transfer energy between the anion valence band and Eu^{3+} is equal to the energy gap between the valence band of the host material and the ground state of Eu^{2+}. Once the Eu^{2+} ground state energy level is assigned, all other energy levels can be predicted according to the trend in binding energies. The energy diagram in Figure 7 uses this method to predict the energy levels of lanthanide ions in bulk II–VI semiconductor materials. In this diagram the charge transfer energy was obtained by using Jörgensen's relationship between the charge transfer energy and the Pauling electronegativity of the anions. 86 For sulfides, selenides and tellurides, we have assumed the charge transfer energy values of 2.17, 2.06 and 0.34 eV respectively. The value (2.17 eV) for sulfide compounds is in good agreement with the assignment of the charge transfer band (~2.43 eV) in the ZnS/Eu system (vide infra). The parameter values in this scheme were obtained from the work of Dorenbos and coworkers 6 and the ground state energies of lanthanides were placed in accordance to the systematic trend of 4f electron binding energies of trivalent lanthanide ions in narrower band gap materials. The energy difference between the 4f ground states of Eu^{3+} and Eu^{2+} was assumed to be 5.70 eV. 4 The higher lying energy levels of Tb^{3+} and Eu^{3+} were placed from the tabulation of Carnall and coworkers for trivalent lanthanide aquo ions. 87،88 The values of the energy levels estimated with this calculation approach compare well to existing data. Wen-lian and coworkers 50 have shown that the Tb^{3+} ground and excited energy levels in ZnS nanoparticles are located at 0.9 eV above the valence band and 0.5 eV below the conduction band, respectively. In a separate study, Chen and coworkers 89 have placed the ground state of Eu^{2+} at 1.6 eV above the valence band of bulk ZnS. Although these values do not match exactly with the values reported in this work, they show sufficiently good qualitative agreement. Considering the typical error of ± 0.5 eV, estimated by Dorenbos, the agreement with the available literature is reasonable. It has to be noted that as long as any systematic error in assigning these energy level values is relatively constant, it should not change the conclusions discussed here.

To determine the charge transfer energy from the anion valence band to Eu^{3+}, the excitation spectra of ZnS/Tb and ZnS/Eu were compared (see figure 8). The band at ~510 nm is assigned to a charge transfer band for Eu^{3+} in the ZnS/Eu system. Note that the red shifted emission spectrum for ZnS/Eu systems with λ_{ex} = 300 nm could arise from its charge transfer nature. Circumstantial evidence for this assignment in the ZnS/Eu system comes from a comparison of Tb^{3+} and Eu^{3+} emission intensities with different excitation wavelengths (see table 4S in supporting information). While the intensity of the Tb^{3+} luminescence decreases sharply when exciting the sample with lower energy than the bandgap of the ZnS nanoparticles, the situation is different for the ZnS/Eu system. Considerable luminescence intensity was observed from Eu^{3+} in ZnS nanoparticles even while exciting the sample at longer wavelength values. Although this observation does not directly prove the existence of a charge transfer band in the ZnS/Eu system, it strongly suggests that some energy level located lower than the bandgap of ZnS nanoparticles exists, and it is involved in the sensitization of Eu^{3+} in the ZnS doped nanoaparticles.

Several features of the energy level diagram in figure 7 are noteworthy.

1. Both the ground and excited states of Tb^{3+} lie within the band gap of bulk ZnS, an effect which should be more pronounced in nanoparticles because of the quantum confinement and hence a higher band gap (~ 4.2 eV as opposed to 3.6 eV for bulk material). This indicates that the Tb^{3+} can potentially act as a hole trap in ZnS. Moreover, it suggests that the excited electron in the $^5D_4$ level of Tb^{3+} does not undergo ready autoionization. These two conditions result in the enhancement of the Tb^{3+} luminescence in ZnS. It is generally believed that the luminescence efficiency of lanthanide ions is increased when their 3+ levels act as trap states. 77

2. The $^5D_4$ level of Tb^{3+} lies above the conduction band of CdSe so that autoionization of the Tb^{3+*} should be efficient, thereby decreasing its luminescence efficiency. Experimentally, the ZnS/Tb^{3+} emission is much stronger than the CdSe/Tb^{3+} emission, for which the overall quantum yields of ZnS/Tb^{3+} and CdSe/Tb^{3+} are 0.12 ± 0.03 and 0.025 ± 0.001 respectively, whereas the Tb^{3+} contribution to the overall quantum yield were found to be 0.05 ± 0.01 and 0.000015 ± 0.000003. It should also be noted that the time-gated mode is required to observe the Tb^{3+} emission in CdSe/Tb^{3+}, 30 whereas they were readily observable in steady-state mode for ZnS/Tb^{3+} luminescence.

3. The energy level locations of Eu^{3+} are qualitatively different from Tb^{3+} in ZnS, as both the ground and excited states of Eu^{3+} lie below the valence band of ZnS. It is important to note that the ground state of Eu^{2+} lies within the band gap of ZnS, which makes the system a potential electron trap. Based on these considerations, Eu^{3+} can be brought to the excited state by two possible pathways: (1) a bandgap transition of the ZnS host and (2) a ZnS valence band to Eu^{2+} ground state transition. Our observations are consistent with either of these mechanisms.

4. ZnS should be more efficient than ZnSe in sensitizing Tb^{3+} luminescence, because as the excited energy level of Tb^{3+} lies close to the conduction band of ZnSe, the excited electrons face a competitive nonradiative path of autoionization. To test this hypothesis ZnSe/Tb nanoparticles were prepared. The measured Tb^{3+} lanthanide-centered quantum yield value for ZnSe/Tb is 0.00018 ± 0.00007 as compared to 0.05 ± 0.01 for ZnS/Tb system, validating this prediction.

5. Based on the energy level diagrams, CdS should be more efficient in sensitizing Tb^{3+} luminescence than is CdSe, but similar or less efficient than ZnS. To check this prediction, experiments with the CdS/Tb system were undertaken. Results from these experiments are shown in figure 9. Sharp Tb^{3+} bands are clearly visible at 490 nm and 545 nm. Interestingly, a band shift in the time-gated excitation spectra with the growth time of nanoparticles is evident and attributed to the effect of quantum confinement. This shift unequivocally points toward the presence of an antennae effect for the Tb^{3+} sensitization. Moreover, based on the ratio of bandgaps and Tb^{3+} emission intensities, it is apparent that the ZnS is more efficient than CdS in sensitizing Tb^{3+} luminescence, which is consistent with the prediction based on the energy level diagrams. The ratio of ZnS bandgap emission to the Tb^{3+} luminescence at ~545 nm in ZnS and CdS was found to be 1:10:1.4.

Conclusion

An efficient and less toxic luminescent lanthanide system, comprised of ZnS nanoparticles with incorporated lanthanide ions, has been established. Efficient sensitization was observed for both the ZnS/Tb^{3+} and the ZnS/Eu^{3+} systems. The ZnS/Tb^{3+} nanoparticles appear to be more efficient lanthanide-based emitters, with lanthanide-centered quantum yield values for ZnS/Tb^{3+} and ZnS/Eu^{3+} being 0.05 ± 0.01 and 0.00013 ± 0.00004 respectively. Excitation spectra, while monitoring the lanthanide emission, clearly reveal that ZnS nanoparticles act

as an antenna to sensitize the lanthanide luminescence in these systems. Moreover, the absence of observable sharp bands in the excitation spectra indicate that direct excitation of lanthanides has a negligible contribution to the overall sensitization mechanism. These systems represent a significant improvement over the originally proposed system CdSe/Tb^{3+}, in their efficiency for lanthanide luminescence sensitization.

The mechanism of lanthanide luminescence sensitization in II–VI semiconductor materials can be rationalized by a semi-empirical method proposed by Dorenbos and coworkers. 1−6 Energy level diagrams indicate that in ZnS, Tb^{3+} can act as a potential hole trap and provide a dramatic increase in sensitization efficiency because its energy levels lie between the nanoparticle band edges. The mechanism of Eu^{3+} luminescence sensitization, on the other hand, follows a different type of mechanism. In ZnS, Eu^{3+} can act as a potential electron trap; hence the sensitization can be achieved either by direct bandgap excitation or by a valence band to Eu^{2+} transition. Either mechanism can explain the experimental observations in the ZnS/Eu system. A comparison of lanthanide efficiency in ZnS nanoparticles is made with respect to other II–VI materials. Emphasis is given to Tb^{3+} doped ZnSe and CdS nanoparticles; both being less efficient than the ZnS nanoparticles in sensitizing the Tb^{3+} luminescence, which is consistent with the predictions based on the energy level positions.

Supplementary Material

Refer to Web version on PubMed Central for supplementary material.

Acknowledgments

We acknowledge financial support from the National Institute of Health, via NIH grant R21-EB008257-01A1. Stéphane Petoud acknowledges support in France from la Ligue contre le Cancer and from Institut National de la Santé et de la Recherche Médicale (INSERM). Prasun Mukherjee and David Waldeck acknowledge partial support from the National Science Foundation (CHE-0718755). We thank Dr. Pieter Dorenbos for useful comments.

References

1. Dorenbos P. J. Phys.: Condens. Matter. 2003; 15:8417–8434.
2. Dorenbos P. J. Lumin. 2004; 108:301–305.
3. Dorenbos P. J. Lumin. 2005; 111:89–104.
4. Dorenbos P, vanderKolk E. Appl. Phys. Lett. 2006; 89:061122-1–061122-3.
5. Dorenbos P, vanderKolk E. Opt. Materials. 2008; 30:1052–1057.
6. Dorenbos P. J. Alloys and Compounds. 2009; 488:568–573.
7. Richardson FS. Chem. Rev. 1982; 82:541–552.
8. Moore EG, Samuel APS, Raymond KN. Acc. Chem. Res. 2009; 42:542–552. [PubMed: 19323456]
9. Hildebrandt N, Löhmannsröben H-G. Curr. Chem. Biol. 2007; 1:167–186.
10. Binnemans K. Chem. Rev. 2009; 109:4283–4374. [PubMed: 19650663]
11. Montgomery CP, Murray BS, New EJ, Pal R, Parker D. Acc. Chem. Res. 2009; 42:925–937. [PubMed: 19191558]
12. Bünzli J-CG. Chem. Rev. 2010; 110:2729–2755. [PubMed: 20151630]
13. Hibon A, Pierre VC. Anal. Bioanal. Chem. 2009; 394:107–120. [PubMed: 19283368]
14. White KA, Chengelis DA, Gogick KA, Stehman J, Rosi NL, Petoud S. J. Am. Chem. Soc. 2009; 131:18069–18071. [PubMed: 19938832]
15. Eliseevaa SV, Bünzli J-CG. Chem. Soc. Rev. 2010; 39:189–227. [PubMed: 20023849]
16. Bünzli J-CG, Piguet C. Chem. Soc. Rev. 2005; 34:1048–1077. [PubMed: 16284671]
17. Carnall, WT.; Fields, PR. Lanthanide/Actinide Chemistry. Vol. Vol. 71. Washington D. C.: American Chemical Society; 1967.

18. Bhargava RN. J. Lumin. 1996; 70:85–94.
19. Brennan JD, Capretta A, Yong K, Gerritsma D, Flora KK, Jones A. Photochem. Photobiol. 2002; 75:117–121. [PubMed: 11883598]
20. Kim YH, Baek NS, Kim HK. Chem. Phys. Chem. 2006; 7:213–221. [PubMed: 16370020]
21. Sato S, Wada M. Bull. Chem. Soc. Jap. 1970; 43:1955–1962.
22. Yang C, Fu L-M, Wang Y, Zhang J-P, Wong W-T, Ai X-C, Qiao Y-F, Zou B-S, Gui L-L. Angew. Chem. Int. Ed. 2004; 43:5010–5013.
23. Chen Y, Lu Z. Anal. Chim. Acta. 2007; 587:180–186. [PubMed: 17386771]
24. Sivakumar S, vanVeggel FCJM, Raudsepp M. Chem. Phys. Chem. 2007; 8:1677–1683. [PubMed: 17583905]
25. Xueyuan C, Wenqin L, Yongheng L, Guokui L. J. Rare Earths. 2007; 25:515–525.
26. Anderson WW. Phys. Rev. 1964; 136:A556–A560.
27. Palm J, Gan F, Zheng B, Michel J, Kimerling LC. Phys. Rev. B. 1996; 54:17603–17615.
28. Klik MAJ, Gregorkiewicz T, Bradley IV, Wells J-PR. Phys. Rev. Lett. 2002; 89:227401-1–227401-4. [PubMed: 12485102]
29. Beeby A, Clarkson IM, Dickins RS, Faulkner S, Parker D, Royle L, deSousa AS, Williams JAG, Woods M. J. Chem. Soc., Perkin Trans. 1999; 2:493–503.
30. Chengelis DA, Yingling AM, Badger PD, Shade CM, Petoud S. J. Am. Chem. Soc. 2005; 127:16752–16753. [PubMed: 16316198]
31. Streetman, BG.; Banerjee, S. Solid State electronic Devices. 5th ed.. New Jersey: Prentice Hall; 2000.
32. Fuhs W, Ulber I, Weiser G, Bresler MS, Gusev OB, Kuznetsov AN, Kudoyarova VK, Terukov EI, Yassievich IN. Phys. Rev. B. 1997; 56:9545–9551.
33. Yassievich I, Bresler M, Gusev O. J. Non-Cryst. Solids. 1998; 226:192–199.
34. Abiko Y, Nakayama N, Akimoto K, Yao T. Phys. Stat. Sol. (b). 2002; 229:339–342.
35. Kühne H, Weiser G, Terukov EI, Kusnetsov AN, Kudoyarova VK. J. Appl. Phys. 1999; 86:896–901.
36. Tsimperidis I, Gregorkiewicz T, Bekman HHPT, Langerak CJGM. Phys. Rev. Lett. 1998; 81:4748–4751.
37. Gregorkiewicz T, Thao DTX, Langer JM, Bekman HHPT, Bresler MS, Michel J, Kimerling LC. Phys. Rev. B. 2000; 61:5369–5375.
38. Kahng D. Appl. Phys. Lett. 1968; 13:210–212.
39. Chen YS, Burgiel JC, Kahng D. J. Electrochem. Soc.: Solid State Science. 1970; 117:794–797.
40. Krupka DC. J. Appl. Phys. 1972; 43:476–481.
41. Świątek K, Godlewsk M. Appl. Phys. Lett. 1990; 56:2192–2194.
42. Świątek K, Suchocki A, Godlewski M. Appl. Phys. Lett. 1990; 56:195–197.
43. Godlewski M, Zakrzewski AJ, Ivanov VY. J. Alloys and Compounds. 2000; 300-301:23–31.
44. Świątek K, Suchocki A, Przybylinska H, Godlewski M. J. Cryst. Growth. 1990; 101:435–438.
45. Godlewski M, Świątek K, Monemar B. J. Lumin. 1994; 58:303–306.
46. Przybylinska H, Godlewski M. Phys. Rev. B. 1987; 36:1677–1682.
47. Przybylińska H, Świątek K, Stapor A, Suchocki A, Godlewski M. Phys. Rev. B. 1989; 40:1748–1755.
48. Świątek K, Godlewski M, Hommel D. Phys. Rev. B. 1990; 42:3628–3633.
49. Chen L, Zhang J, Lu S, Ren X, Wang X. Chemical Physics Letters. 2005; 409:144–148.
50. Jing-hua N, Rui-nian H, Wen-lian L, Ming-tao L, Tian-zhi Y. J. Phys. D: Appl. Phys. 2006; 39:2357–2360.
51. Dong L, Liu Y, Zhuo Y, Chu Y. Eur. J. Inorg. Chem. 2010:2504–2513.
52. Hou S, Yuen Y, Mao H, JiqingWang, Zhu Z. J. Phys. D: Appl. Phys. 2009; 42 215105.
53. Wang L, Xu X, XinYuan. J. Lumin. 2010; 130:137–140.
54. Planelles-Aragó J, Julián-López B, Cordoncillo E, Escribano P, Pellé F, Viana B, Sanchez C. J. Mater. Chem. 2008; 18:5193–5199.

55. Ehrhart G, Capoen B, Robbe O, Beclin F, Boy P, Turrell S, Bouazaoui M. Optical Materials. 2008; 30:1595–1602.
56. Yang H, Yu L, Shen L, Wang L. Materials Letters. 2004; 58:1172–1175.
57. Chen W, Joly AG, Malm J-O, Bovin J-O. J. Appl. Phys. 2004; 95:667–672.
58. Qu SC, Zhou WH, Liu FQ, Chen NF, Wang ZG, Pan HY, Yu DP. Appl. Phys. Lett. 2002; 80:3605–3607.
59. Bol AA, Beek Rv, Meijerink A. Chem. Mater. 2002; 14:1121–1126.
60. Sun XL, Zhang GL, Tang GQ, Chen WJ. Chin. Chem. Lett. 1999; 10:807–810.
61. Sun L, Yan C, Liu C, Liao C, Li D, Yu J. Journal of Alloys and Compounds. 1998; 275–277:234–237.
62. Kallmann H, Luchner K. Phys. Rev. 1961; 123:2013–2019.
63. Luchner KM, Kallmann HP, Kramer B, Wachter P. Phys. Rev. 1963; 129:593–596.
64. Meech SR, Phillips DC. J. Photochem. 1983; 23:229–235.
65. Petoud S, Cohen SM, Bünzli J-CG, Raymond KN. J. Am. Chem. Soc. 2003; 125:13324–13325. [PubMed: 14583005]
66. Brus LE. J. Chem. Phys. 1984; 80:4403–4409.
67. Sooklal K, Cullum BS, Angel SM, Murphy CJ. J. Phys. Chem. 1996; 100:4551–4555.
68. Li LS, Pradhan N, Wang Y, Peng X. Nano Lett. 2004; 4:2261–2264.
69. Chen W, Wang Z, Lin Z, Lin L. J. Appl. Phys. 1997; 82:3111–3115.
70. Here we wish to comment on the presence of Eu^{2+} in the ZnS/Eu samples. While working on an extensive tabulation of charge transfer energies to Eu^{3+} in different inorganic materials, Dorenbos could not find any literature information of this data in sulfides. [reference 3] In a previous study, Blasse et al. concluded that for systems in which E_{CT} (Eu^{3+}) < 2.5 eV, Eu^{3+} is not the stable valence state. [Mater. Chem. Phys. 1987, 16, 237–252] The unavailability of this parameter value was taken to be an indication of Eu^{2+} being the stable valence state for Eu compounds where $E_{CT} < E_F$, E_F being the Fermi energy level. [reference 3] However, Dorenbos did not exclude the possibility of the existence of Eu^{3+} state in sulfides exclusively. [reference 3] The luminescence from Eu^{3+} ions in sulfide systems is known. [references 52⁻56, 60⁻61] The absence of broad emission with band maximum centered at ~520 nm upon exciting the sample at ~300 nm indicates that the samples under investigation in the present work do not have evident spectral contribution from Eu^{2+}. With l_{ex} = 260 nm Chen and coworkers have reported a broad emission of Eu^{2+} in ZnS/Eu^{2+} nanoparticles with the band maximum located at ~530 nm and assigned it to the allowed $4f^6 5d\text{-}4f^7$ transition. [reference 89] Similar broad Eu^{2+} emission was also observed by Shu-Man and coworkers in Eu doped ZnS nanoparticles with band maximum located at ~520 nm. [Chin. Phys. Lett. 2000, 17, 609–611].
71. Fonoberov VA, Balandin AA. Appl. Phys. Lett. 2004; 85:5971–5973.
72. Chestnoy N, Harris TD, Hull R, Brus LE. J. Phys. Chem. 1986; 90:3393–3399.
73. Petoud S, Muller G, Moore EG, Xu J, Sokolnicki J, Riehl JP, Le UN, Cohen SM, Raymond KN. J. Am. Chem. Soc. 2007; 129:77–83. [PubMed: 17199285]
74. Lakowicz, JR. Principles of Fluorescence Spectroscopy. Third ed..
75. It has been assumed that both the nanoparticles have similar luminescence lifetime in absence of acceptors and Tb^{3+} resides at almost equal distance from the nanoparticle sensitizing center.
76. Whitney PS, Uwai K, Nakagome H, Takahei K. Appl. Phys. Lett. 1988; 53:2074–2076.
77. Takahei K, Taguchi A, Nakagome H, Uwai K, Whitney PS. J. Appl. Phys. 1989; 66:4941–4945.
78. Thonke K, Pressel K, Bohnert G, Stapor A, Weber J, Moser M, Molassioti A, Hangleiter A, Scholz F. Sernicond. Sci. Technol. 1990; 5:1124–1131.
79. Needels M, Schlüter M, Lannoo M. Phys. Rev. B. 1993; 47:15533–15536.
80. Lazarides T, Tart NM, Sykes D, Faulkner S, Barbieri A, Ward MD. Dalton Trans. 2009:3971–3979. [PubMed: 19440596]
81. Pedrini, C.; Bouttet, D.; Dujardin, C.; Belsky, A.; Vasil'ev, A. Dorenbos, P.; van Eijk, CWE., editors. The Netherlands: Delft University Press; 1996. p. 103
82. Sato S. J. Phys. Soc. Jpn. 1976; 41:913–920.

83. Thiel CW, Gruguel H, Wu H, Sun Y, Lapeyre GJ, Cone RL, Equall RW, Macfarlane RM. Phys. Rev. B. 2001; 64:085107-1–085107-13.

84. Thiel CW, Gruguel H, Sun Y, Lapeyre GJ, Macfarlane RM, Equall RW, Cone RL. J. Lumin. 2001; 94/95:1–6.

85. Thiel CW, Sun Y, Cone RL. J. Mod. Opt. 2002; 49:2399–2411.

86. Jörgensen, CK. Modern Aspects of Ligand Field Theory. North-Holland: Amsterdam; 1971.

87. Carnall WT, Fields PR, Rajnak K. J. Chem. Phys. 1968; 49:4447–4449.

88. Carnall WT, Fields PR, Rajnak K. J. Chem. Phys. 1968; 49:4450–4455.

89. Chen W, Malm J-O, Zwiller V, Huang Y, Liu S, Wallenberg R, Bovin J-O, Samuelson L. Phys. Rev. B. 2000; 61:11021–11024.

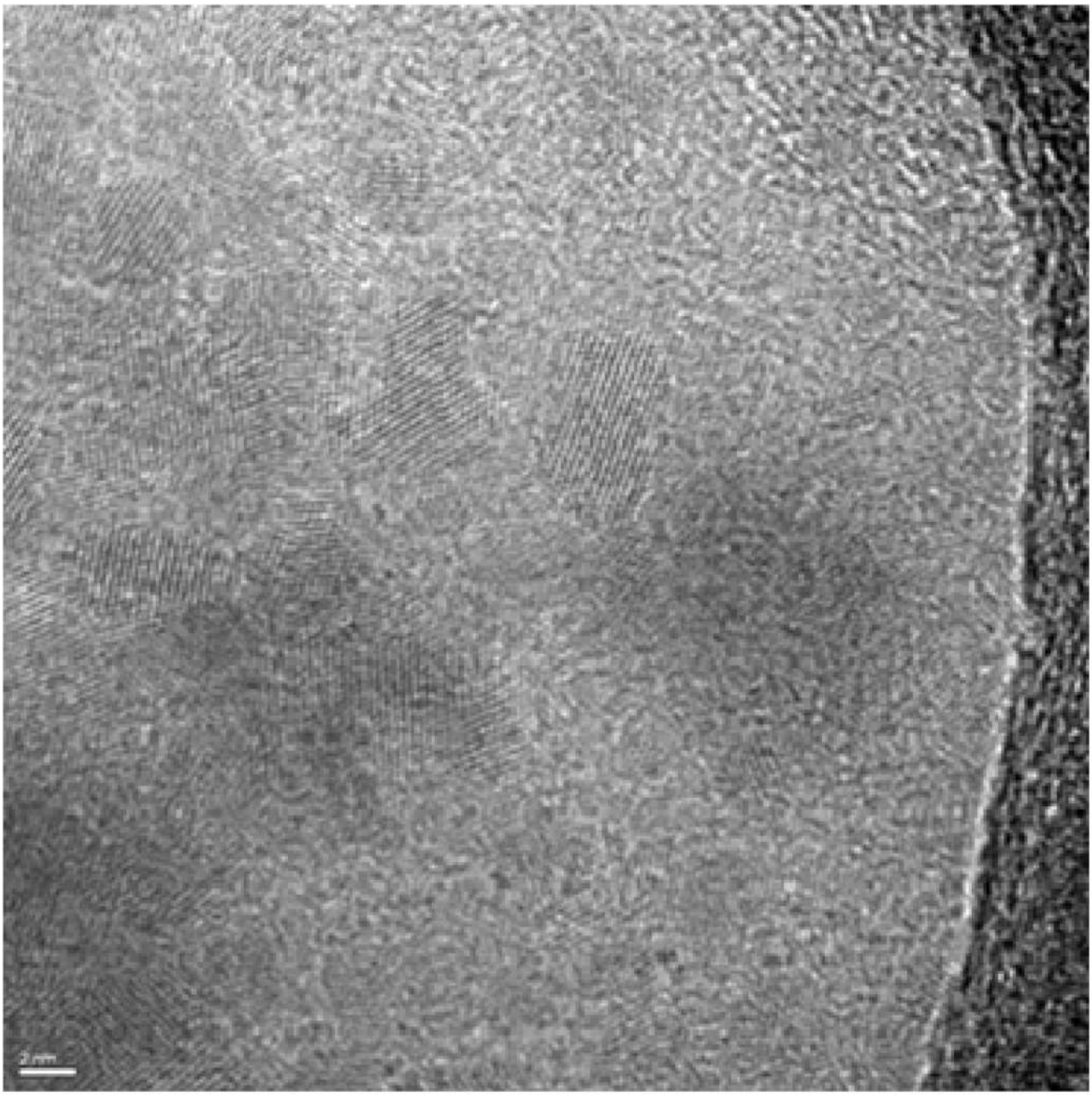

Figure 1.
Representative HRTEM image of synthesized ZnS/Tb nanoparticles. A 2 nm scale bar is shown on the bottom left of the image.

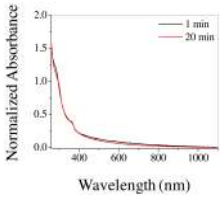

Figure 2.

Representative normalized absorption spectra of a ZnS nanoparticle sample dissolved in chloroform obtained with growth times of 1 minute and 20 minutes. Spectra were normalized arbitrarily at 295 nm. The band at ~290 nm is associated with the band gap transition (see text).

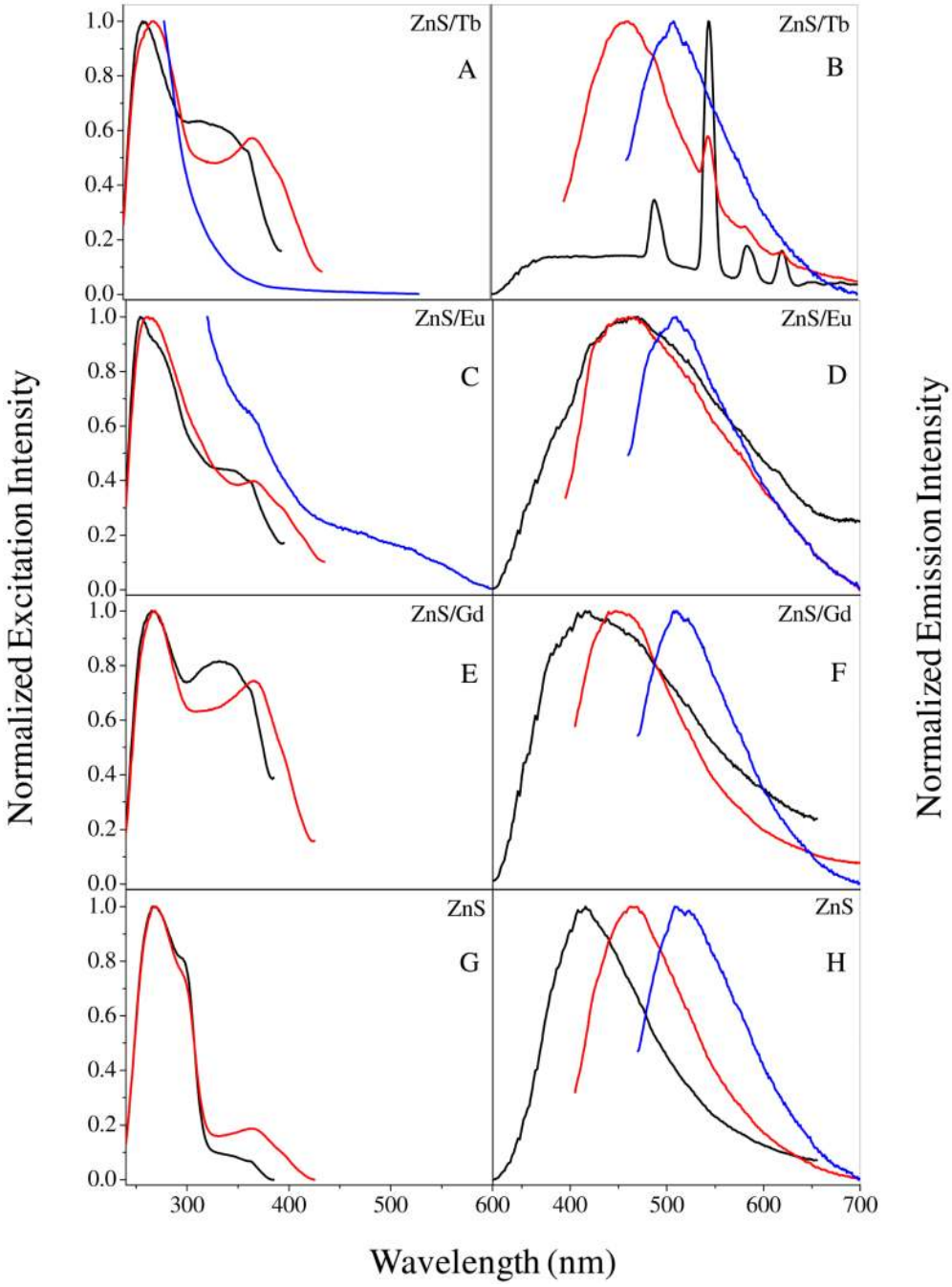

Figure 3.

Left Panel: Normalized excitation spectra for λ_{em} = 410 nm (black), 450 nm (red), and 545 nm (blue) (only for ZnS/Tb); and 620 nm (blue) (only for ZnS/Eu). Right Panel: Normalized emission spectra for λ_{ex} = 300 nm (black), 375 nm (red), and 440 nm (blue). All of the spectra are taken in chloroform.

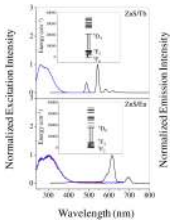

Figure 4.

Normalized time-gated excitation and emission spectra of ZnS/Tb [λ_{ex} = 300 nm (black), λ_{em} = 490 nm (red), λ_{em} = 545 nm (blue)] (upper panel) and ZnS/Eu [λ_{ex} = 300 nm (black), λ_{em} = 616 nm (red), λ_{em} = 696 nm (blue)] nanoparticle samples in chloroform. Inset shows the electronic transitions associated with the 490 nm and 545 nm bands for ZnS/Tb, 616 nm and 696 nm bands for ZnS/Eu.

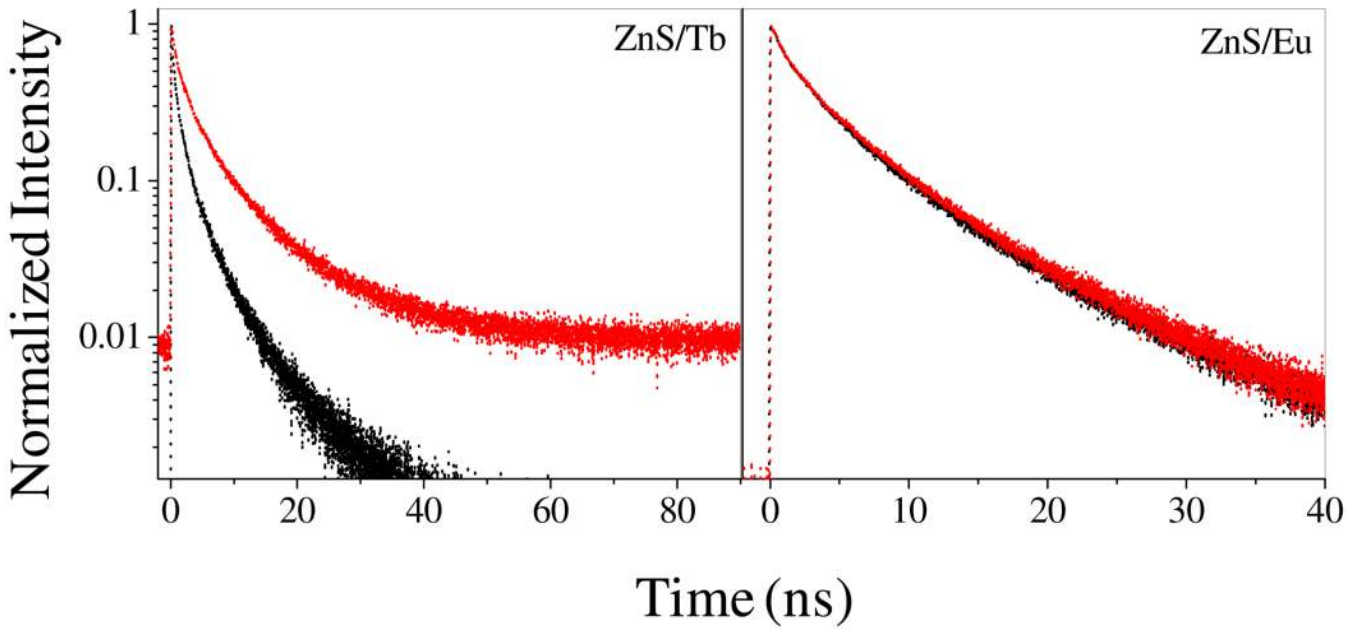

Figure 5.

Representative luminescence decay plots are shown for different nanoparticle systems studied in chloroform. For ZnS/Tb the black curve is at λ_{em} = 400 nm (no Tb^{3+} emission) and the red curve is at λ_{em} = 545 nm. For ZnS/Eu the black curve is λ_{em} = 500 nm (no Eu^{3+} emission) and the red curve is λ_{em} = 618 nm. Luminescence decay parameters are summarized in tables 1S and 2S. The traces that have been recorded with a time windows that can only give information on nanoparticle electronic structure decay kinetics as they have shorter emission lifetimes.

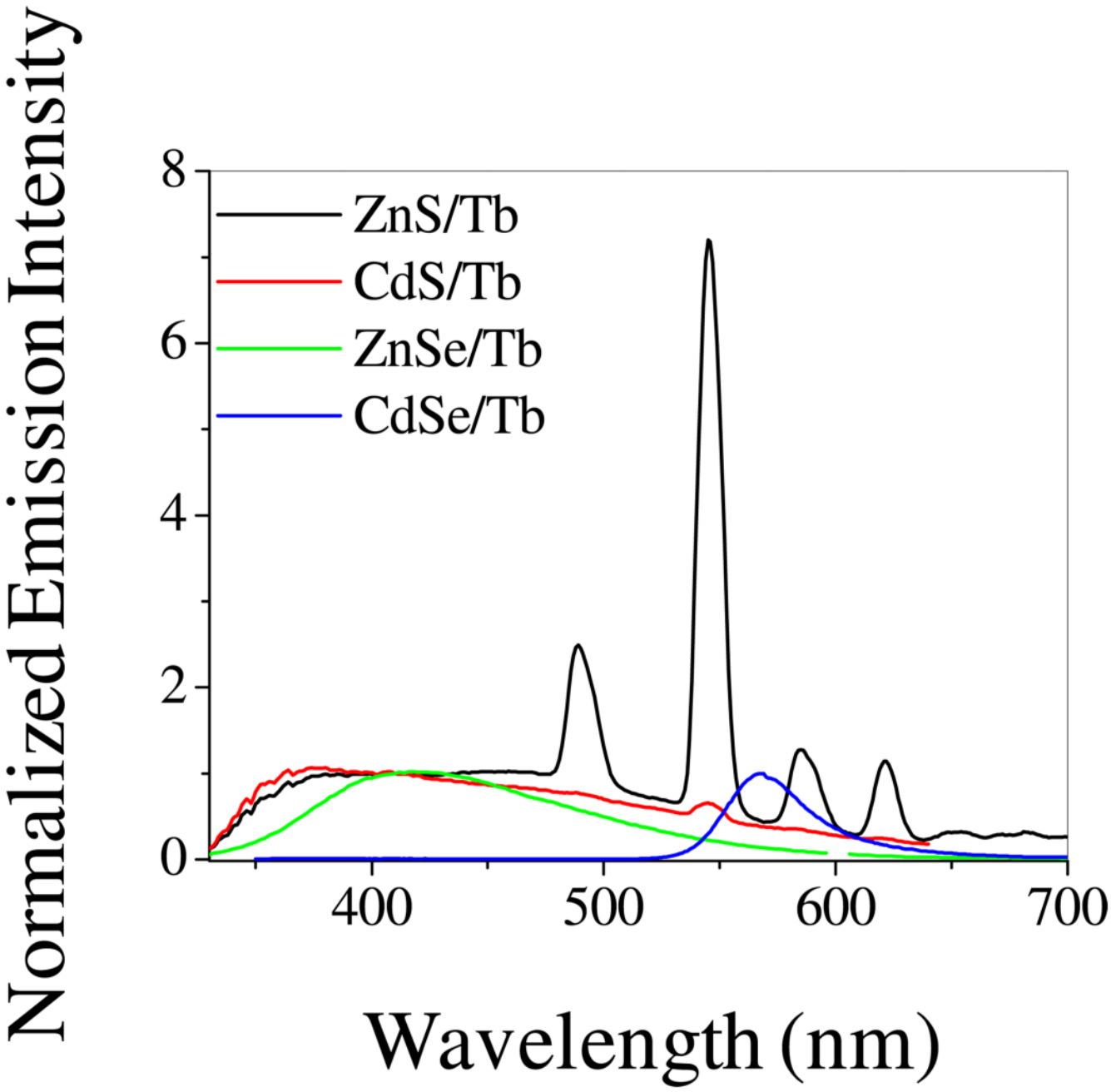

Figure 6.

Emission spectra of different systems studied with $\lambda_{ex} \approx 300$ nm. The ZnS/Tb (black), CdS/Tb (red) and ZnSe/Tb (green) spectra are normalized to unity at 410 nm and the CdSe/Tb spectrum (blue) is normalized to unity at the band position. These spectra clearly put in evidence the difference in Tb^{3+} luminescence sensitization efficiency by different types of nanoparticles.

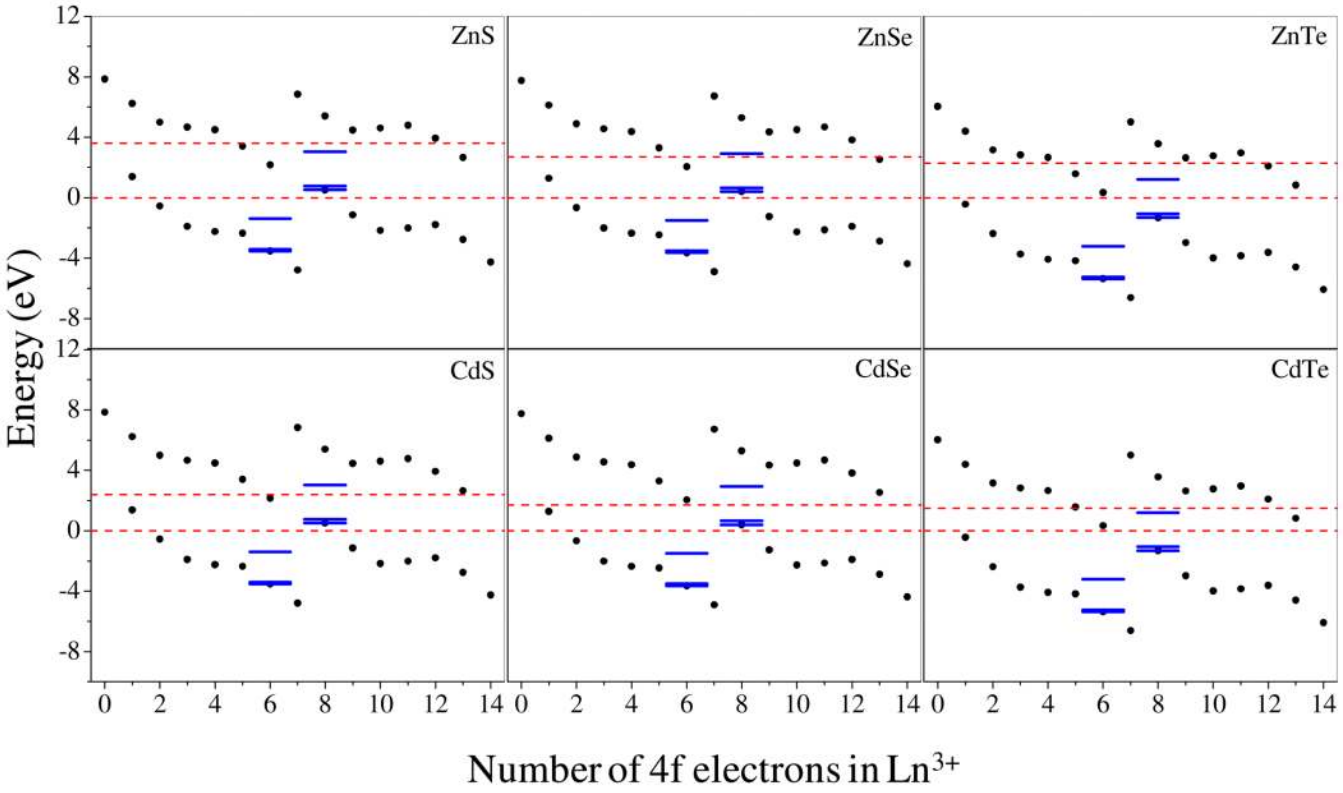

Figure 7.

Energy level diagram of lanthanide (III) ions in different II–VI semiconductor materials based on the method proposed by Dorenbos. 1⁻6 At each abscissa value, the lower and higher solid circles are the ground state energy of lanthanide (III) and lanthanide (II) ions respectively. The blue solid horizontal lines at× = 6 and 8 represents the ground and excited states of Eu^{3+} and Tb^{3+} ions. The red dashed lines represent the bulk band gap values; the valence band energy is arbitrarily set at zero. It is worth noting that Tb^{3+} is a potential hole trap in II–VI sulfide and selenide compounds and Eu^{3+} can potentially act as an electron trap in these compounds.

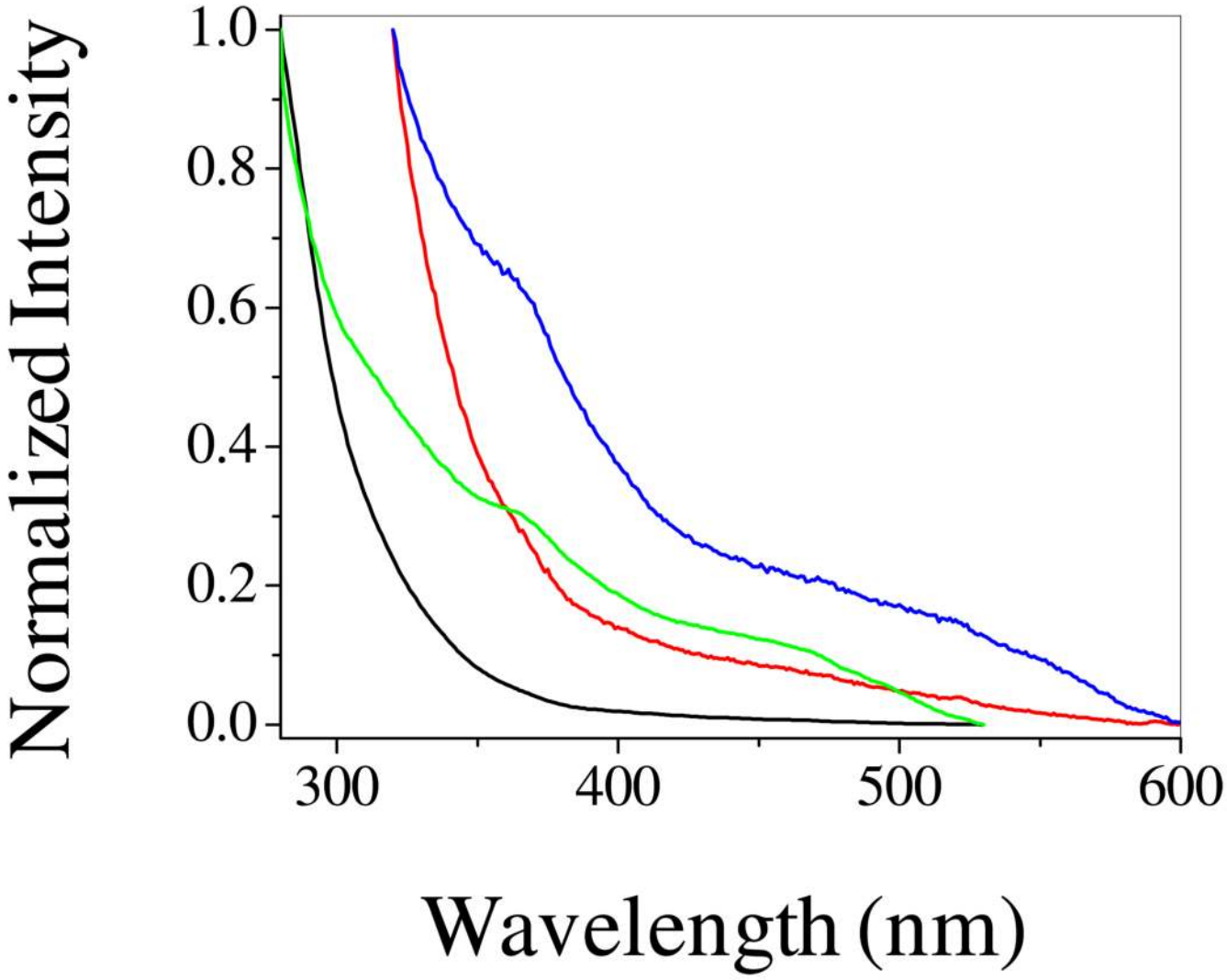

Figure 8.
Normalized steady-state excitation spectra of ZnS/Tb nanoparticles with λ_{em} = 545 nm (black) and 620 nm (red). The green and blue curves are the corresponding spectra for ZnS/Eu nanoparticles. Spectra are normalized arbitrarily to the maximum intensity.

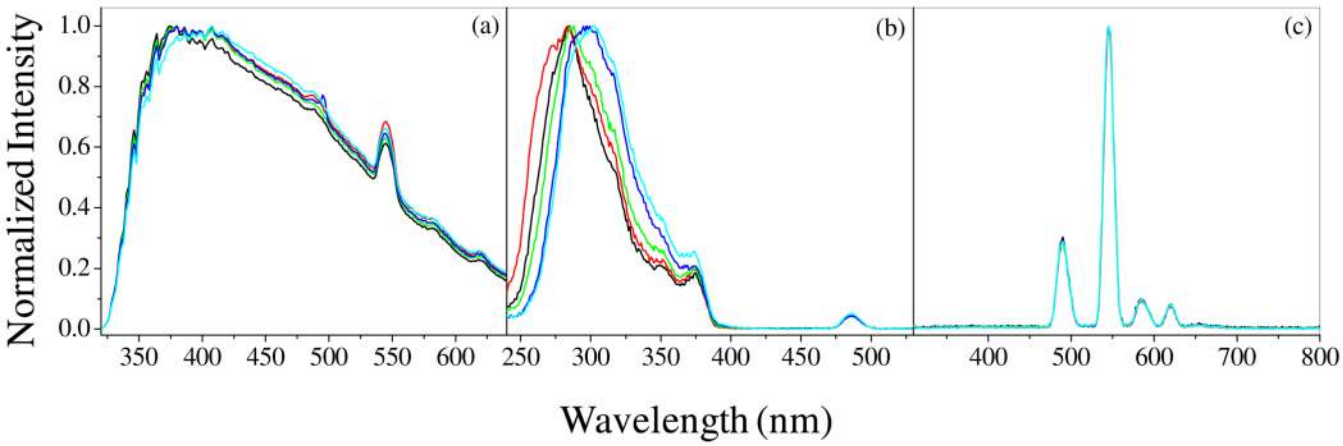

Figure 9.

Normalized (a) steady-state emission with λ_{ex} = 300 nm, (b) time-gated excitation with λ_{em} = 545 nm and (c) time-gated emission with λ_{ex} = 300 nm of CdS nanoparticles in chloroform with 1 minute (black), 2 minutes (red), 5 minutes (green), 10 minutes (blue) and 20 minutes (cyan) growth times. Intensities of the excitation and emission spectra are normalized to the highest intensity of the respective spectra. Sharp Tb^{3+} bands are clearly visible in the steady-state mode. We observe a band shift in the excitation spectra monitoring the Tb^{3+} emission band, which undoubtedly confirms the presence of the antennae effect between the electronic structure of the nanoparticle and Tb^{3+}.